AGU100 ADVANCING EARTH AND SPACE SCIENCE

JGR

Journal of Geophysical Research: Oceans

RESEARCH ARTICLE
10.1029/2018JC013984

Key Points:
- To correctly model transport through the CAA, ice velocity, and probably landfast ice, needs to be properly represented in numerical models
- Increasing surface stress reduces the flow through the Queen Elizabeth Islands but increases the flow through the central and southern CAA
- Freshwater transport is more sensitive to surface stress changes than volume transport

Correspondence to:
N. Grivault,
grivault@ualberta.ca

Citation:
Grivault, N., Hu, X., & Myers, P. G. (2018). Impact of the surface stress on the volume and freshwater transport through the Canadian Arctic Archipelago from a high-resolution numerical simulation. *Journal of Geophysical Research: Oceans*, *123*, 9038–9060. https://doi.org/10.1029/2018JC013984

Received 23 MAR 2018
Accepted 7 NOV 2018
Accepted article online 14 NOV 2018
Published online 13 DEC 2018

Impact of the Surface Stress on the Volume and Freshwater Transport Through the Canadian Arctic Archipelago From a High-Resolution Numerical Simulation

Nathan Grivault[1], **Xianmin Hu**[1,2], **and Paul G. Myers**[1]

[1]Department of Earth and Atmospheric Sciences, University of Alberta, Edmonton, Alberta, Canada, [2]Now at Bedford Institute of Oceanography, Dartmouth, Nova Scotia, Canada

Abstract We use a numerical model forced with high temporal and spatial resolution atmospheric forcing to evaluate the volume and freshwater transport through the Canadian Arctic Archipelago (CAA). On average, the simulated inflow through the Queen Elizabeth Islands represents 40% of the transport entering the CAA through M'Clure Strait. The transport through Admunsden Gulf represents less than 10% of the total inflow. The impact of sea ice and winds on the volume and freshwater transports into and through this region is also investigated. At Nares Strait and West Lancaster Sound, the transport is overestimated due to too-mobile sea ice but different physical processes related to surface stress. The ice is driving larger ocean flow in the first case, while causing less flow reduction in the second case. While the transport through the Queen Elizabeth Islands responds to the changes in surface stress over the Beaufort Gyre and northern Baffin Bay, local surface stress opposed to the mean flow over the straits tends to reduce the throughflow transport. In Parry Channel and the southern CAA, the surface stress tends to enhance the transport and have a greater impact locally. Finally, the surface stress related to sea ice motion can significantly change the transport in the CAA during the winter months.

Plain Language Summary We use a numerical computer model including high temporal and spatial resolution atmospheric forcing to evaluate the amount of water and freshwater flowing through the Canadian Arctic Archipelago (CAA). On average, we show that the inflow through the Queen Elizabeth Islands represents about slightly less (40%) than M'Clure Strait, which has historically been considered to be the main source of the inflow. We also show that the flow through the Amundsen Gulf is low (10% of the total), in agreement with previous studies. In addition, we demonstrate how the sea ice motion drives too much flow through West Lancaster Sound and Nares Strait and show the importance of the sea ice motion on the water and freshwater flows through key gates in and out of the CAA. This provides hints on how the dynamics of the flow through the CAA might change in the future with less sea ice cover in a warming world. The flux of freshwater through the CAA is potentially important as it may impact deep water formation in the Atlantic Ocean.

1. Introduction

The Canadian Arctic Archipelago (CAA) is a tangle of shallow basins and narrow straits that connect the Arctic Ocean to Baffin Bay and then the North Atlantic. It is composed of two main regions. One is the Queen Elizabeth Islands (QEI; or Sverdrup Basin) in the north, which is an area with relatively small islands surrounded by the larger Ellesmere, Devon, Cornwallis, Bathurst, Melville, and Prince Patrick Islands (Figure 1). The other region is the southern CAA, which is composed of larger islands (Bank, Victoria, and Prince of Wales Islands). Between the two regions, Parry Channel directly connects the Beaufort Sea to Baffin Bay.

Due to the harsh weather and thick sea ice that covers the archipelago most of the year, it is difficult to access the northern part of the CAA, even in summer. Therefore, very few long-term mooring-based observations are available in the CAA. Based on numerical studies (Kliem & Greenberg, 2003; Lu et al., 2014; McGeehan & Maslowski, 2012; Wang et al., 2012; Wekerle et al., 2013; Zhang et al., 2016), it is known that a weak inflow occurs through the QEI, while the main flow is through the relatively wide passage, that is, Parry Channel, present between the QEI and the southern CAA. The main flow enters Parry Channel from the west M'Clure Strait (90 km wide, sill at $\sim$ 350 m). It continues to the east until it reaches the shallow sill at the end of the

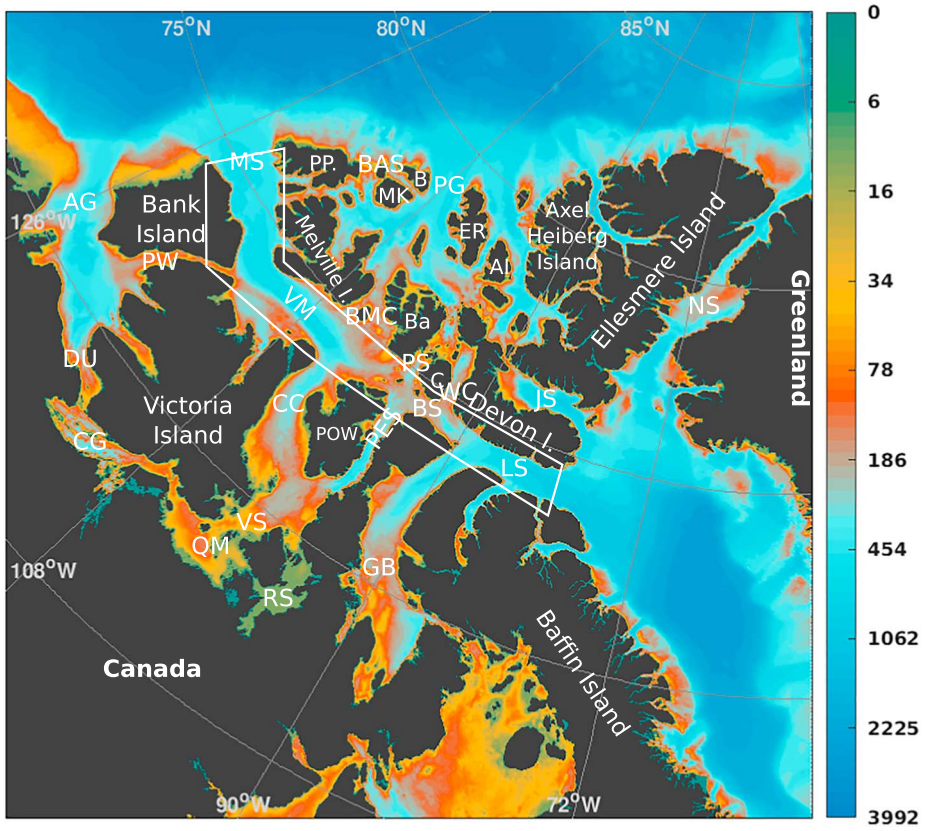

Figure 1. Map of the Canadian Arctic Archipelago. AG = Amundsen Gulf; MS = M'Clure Strait; BAS = Ballantyne Strait; PG = Prince Gustaf Adolf Strait; BMC = Byam Martin Channel; PS = Penny Strait; WC = Wellington Channel; DU = Dolphin Union Strait; VM = Viscount Melville Strait; CC = M'Clintock Channel; PES = Peel Sound; VS = Victoria Strait; RS = Rae Strait; QM = Queen Maud Strait; JS = Jones Sound; NS = Nares Strait; LS = Lancaster Sound; BS: = Barrow Strait; GB = Gulf of Boothia; CG = Coronation Gulf; B = Baden Island; MK = Mackenzie King Island; PP = Prince Patrick Island; Ba = Bathurst Island; C = Cornwallis Island; AI = Amund Ringnes Island; POW = Prince of Wales Island. The color map indicates the model domain bathymetry in meters. The white square corresponds to the Parry Channel.

Viscount Melville Sound (110 km wide). Then, the flow curves to the south into M'Clintock Channel, around Prince of Wales Island and turns north back to Parry Channel at Barrow Strait (60 km wide, sill at ~ 150 m) through Peel Sound (Wang et al., 2012). This flow enters Baffin Bay via Lancaster Sound at the east end of Parry Channel. The Arctic outflow enters Baffin Bay also through Jones Sound and Nares Strait.

The CAA (via Lancaster Sound, Nares Strait, and Jones Sound) is the main pathway of liquid freshwater from the Arctic Ocean to the Northern Atlantic with an annual mean flux of about 100 mSv (1 mSv = $10^3 m^3/s$; reference salinity: 34.8; Melling et al., 2008; Münchow, 2016; Prinsenberg et al., 2009). Relatively, solid freshwater export through the CAA is small (6 mSv; Tang et al., 2004). This freshwater can affect local circulation within Baffin Bay (e.g., Castro de la Guardia et al., 2015; Grivault et al., 2017). Combined with other freshwater sources (e.g., Greenland meltwater), the freshwater leaving Baffin Bay to the south through Davis Strait is 72 to 130 mSv based on mooring observations (Cuny et al., 2005; Curry et al., 2011, 2014). Eventually, it will arrive in the Labrador Sea, where Labrador Sea Water forms. Consequently, it may impact the large-scale oceanic circulation by affecting the upper limb of the Atlantic Meridional Overturning Circulation (Yang et al., 2016). In addition to the Arctic outflow, the river discharge from the main islands contribute about 6 mSv from May to October (i.e., when not covered by ice), based on a study by Spence and Burke (2008).

The current consensus on the CAA dynamics is that the mean flow is controlled by the baroclinic gradient between the Beaufort Gyre and northern Baffin Bay (e.g., Kliem & Greenberg, 2003; Prinsenberg & Bennett, 1987; Wang et al., 2017; Wekerle et al., 2013) while the high frequency variability is driven by wind (e.g., Peterson et al., 2012). Jahn et al. (2009) and Houssais and Herbaut (2011) also found a correlation between large-scale atmospheric patterns (i.e., North Atlantic Oscillation) and the transport through the CAA. Linking

the CAA throughflow to large-scale atmospheric circulation is consistent with a recent study done by Manucharyan et al. (2016), which proposed that the large-scale wind forcing over the Beaufort Gyre leads to the accumulation or release of freshwater, based on the direction of the winds.

As an important freshwater outflow from the Arctic Ocean to the Northern Atlantic, however, the exact amount of volume and freshwater export through the CAA is still an open question. A summary of previous studies is present in Table 1. Mooring data are available at West Lancaster Sound from 1998 to 2010 (Peterson et al., 2012; Prinsenberg et al., 2009) and Nares Strait from 2004 to 2006 and from 2007 to 2009 (Münchow, 2016; Münchow & Melling, 2008). These observations measured a mean volume (freshwater) flow of about 0.46 Sv (32 mSv) at Lancaster Sound (Peterson et al., 2012). At Nares Strait, the transports are about 0.67 Sv (29.6 mSv) and 1.03 Sv (49 mSv) for 2004–2006 and 2007–2009, respectively (Münchow, 2016). Numerical models for the same sections show various amount of transport, usually larger than the observations, with volume (freshwater) transports between 0.46 and 1.15 Sv (32 to 55 mSv) at Lancaster Sound and between 0.81 and 1.4 Sv (25 to 70 mSv) at Nares Strait (Lu et al., 2014; McGeehan & Maslowski, 2012; Shroyer et al., 2015; Wang et al., 2017; Wekerle et al., 2013; Zhang et al., 2016). We note that the impact of tides is not included in the previously given transports. The tidal current will impact the short time scale transport as well as the overall mixing in the CAA, which is significant for the representation of Polynyas in the region (e.g., Hannah et al., 2009).

Another important hydrographic process within the CAA is sea ice. The maximum sea ice extent occurs in May, while the minimum occurs in October (Parkinson & Cavalieri, 2008). Landfast ice (i.e., no motion, fully ice covered) is present in the QEI region between October and November and late July. In the western QEI landfast ice is observed even during summer (Galley et al., 2012; Melling, 2002). In the central CAA, most of the sea ice is landfast by the end of January, while M'Clure Strait, Amundsen Gulf, and eastern Parry Channel have mobile ice in some years (Galley et al., 2012). The breakup of landfast ice starts from June in the southern CAA and then moves toward the central CAA from the periphery until the end of the summer (Galley et al., 2012). Sea ice extent in summer varies significantly from year to year. While sea ice extends across Parry Channel to the southern part of the CAA, a fully open Parry Channel is already observed during the lowest sea ice extent years, such as 2007 and 2012 (Parkinson & Cavalieri, 2008; Stroeve et al., 2007).

The thickness of the sea ice in the CAA is also an open question. Based on drill hole measurements conducted in the 1970s winters, the average ice thickness over the northern CAA is estimated to be about 3 m (Melling, 2002). The ice is often classified by its age, with first-year ice (FYI) having a thickness up to 2.2 m while the multiyear ice (MYI) is thicker. The Northwest CAA is one of the last bastions of thick MYI in the Arctic, with a thickness of up to 5.5 m in winter (Melling, 2002). Most MYI present in the CAA is located in the QEI, while the southern CAA is mainly covered with FYI. The transition between MYI and FYI occurs in Viscount Melville Strait and M'Clintock Channel (Howell et al., 2009; Melling, 2002). Recent observation from Nares Strait showed a median ice draft of about 0.8 m with a significant interannual variability, while MYI of more than 5 m are present (Ryan & Münchow, 2017).

Sea ice area and thickness have decreased dramatically over the last decades (e.g., Comiso, 2012; Kwok & Rothrock, 2009; Parkinson & Cavalieri, 2008; Parkinson & Comiso, 2013; Stroeve et al., 2007). In the CAA, the sea ice area is decreasing at a rate of about 8.7% per decade (Howell et al., 2009) and the concentration at a rate of about 2 per decade (Comiso et al., 2017). The sea ice melt period has increased by 7 days per decade (Howell et al., 2009). MYI volume has decreased at the rate of 6.4% per decade (Comiso, 2012), while record sea ice thickness decreases have been observed, at Cambridge Bay (-4.31 ± 1.4 cm per decade), Eureka (-4.65 ± 1.7 cm per decade), and Alert (-4.44 ± 1.6 cm per decade; Howell et al., 2016). These changes did not impact Nares Strait during the last decade (Ryan & Münchow, 2017). Changes in CAA sea ice could impact the overall freshwater fluxes toward the Northern Atlantic.

In the present paper, we pursue two main goals: (1) to evaluate modeled volume and freshwater transports through the CAA and (2) to understand the impact of the sea ice and wind on modeled volume and freshwater transports through the CAA. To achieve these goals, a high-resolution eddy-permitting regional simulation is conducted, based on a structured ocean-sea-ice-coupled model. The simulation is also driven by high temporal and spatial resolution atmospheric forcing.

Table 1
Summary of the Volume (Sv) and Freshwater (mSv) Transports Through the Canadian Arctic Archipelago

Panel	Section name	Volume transport	Freshwater transport	Source
(a)	Ballantyne + Prince Gustaf Adolf Straits	0.12	5.96	This study
(b)	Ellef Ringnes – Axel Heiberg Island Strait	0.03	1.95	This study
(c)	Central QEI	0.01	1.07	This study
(d)	Prince Patrick Island – Melville Island Strait	−0.05	3.92	This study
(e)	Byam Martin Channel	0.17	10.63	This study
	1958–2007	0.27	22	Wekerle et al. (2013)
	1982–1984	**0.12**		Fissel (1988)
(f)	Penny Strait + Wellington Channel	0.03	1.16	This study
	1958–2007	0.09[a]	7[a]	Wekerle et al. (2013)
	1982–1984	**0.29**		Fissel (1988)
(g)	Lancaster Sound	0.58	44.13	This study
	1988–2007	1.15	55	Lu et al. (2014)
	1958–2007	0.86	71	Wekerle et al. (2013)
	1978–2013	0.71		Zhang et al. (2016)
	1998–2010	**0.46**	**32**	Peterson et al. (2012)
	1982–1984	**0.45**		Fissel (1988)
	1928	**0.65**		Kiilerich (1939)
	1954	**1.50**		Bailey (1957)
	1954	**1.00**		Collin (1962)
	1966	**0.45**		Palfrey and Day (1968)
(h)	M'Clure Strait	0.40	27.47	This study
	1958–2007	0.45	40	Wekerle et al. (2013)
	1982–1984	**0.05**		Fissel (1988)
(I)	Prince of Wales Strait	−0.05	−6.02	This study
	1958–2007	0.01	2	Wekerle et al. (2013)
	1982–1984	**0.05**		Fissel (1988)
(j)	Mc Clintock Channel	0.21	17.17	This study
	1958–2007	0.27	24	Wekerle et al. (2013)
	1982–1984	0.06		Fissel (1988)
(k)	Peel Sound	−0.22	−23.62	This study
	1958–2007	−0.29	−26	Wekerle et al. (2013)
(l)	Gulf of Boothia	0.03	4.46	This study
(m)	Amundsen Gulf	0.05	3.90	This study
(n)	Victoria Strait	0.00	−4.56	This study
(o)	Jones Sound	0.00	−0.03	This study
	1978–2013	0.31		Zhang et al. (2016)
	1928	**0.30**		Kiilerich (1939)
	1954	**−0.40**		Bailey (1957)
	1954	**0.25**		Collin (1962)
	1966	**0.30**		Palfrey and Day (1968)
(p)	Nares Strait	0.89	42.77	This study
	1988–2007	1.14	25	Lu et al. (2014)
	1958–2004	1.40	77	Wang et al. (2017)
	1978–2007	0.91	48	Wekerle et al. (2013)
	1978–2013	0.81		Zhang et al. (2016)
	1998–2010	0.16		Peterson et al. (2012)
	2003–2009	**0.85**	**39**	Münchow (2016)

Table 1 (*continued*)

Panel	Section name	Volume transport	Freshwater transport	Source
	1928	**0.4**[b]		Kiilerich (1939)
	1954	**−0.4**[b]		Bailey (1957)
	1966	**0**[b]		Palfrey and Day (1968)

Note. Transports are averaged from November 2003 to December 2016 in this study. The averaging period for other studies is specified. The panel letters corresponds to the straits shown in Figure 9. Bold numbers are from observations.
[a]Includes only Penny Strait. [b]Data from Smith Sound.

This paper is structured as follows. Section 2 describes the model configuration and the observations used in this study. Section 3 presents the model evaluation over the CAA. The impact of sea ice on the transport is investigated in section 4. Finally, conclusions are given in section 5.

2. Method

2.1. Numerical Model

In this study we use the Nucleus for European Modeling of the Ocean (NEMO) numerical framework, version 3.4. This coupled ocean and sea ice model includes a three-dimensional, free-surface, hydrostatic, primitive-equation ocean component and a dynamic-thermodynamic sea ice model (Madec, 2008). The sea ice model is from the Louvain-la-Neuve sea ice model (Vancoppenolle et al., 2009) with a modified elastic-viscous-plastic ice rheology (Hunke, 2001). The vertical diffusivity and viscosity coefficients are computed by a turbulent closure scheme based on the prognostic equation for the turbulent kinetic energy (Blanke & Delecluse, 1993) modified by Madec et al. (1998). Horizontal tracer diffusivity and viscosity use a Laplacian operator ($A^t \Delta T$, where $A^t = 300$ m^2/s is the tracer mixing coefficient), while a bi-Laplacian operator is used for the momentum ($A^{\mathbf{u}} \Delta^2 \mathbf{u}$, where $A^{\mathbf{u}} = -1.5 \times 10^{11}$ m^4/s is the maximum velocity mixing coefficient). The bottom friction is based on a nonlinear relationship dependent on the bottom velocity with a drag coefficient of 1.0×10^{-3}. The fast frequency variation of the free surface has been filtered out. The model time step is 180 s. Note that the experiment does not include tides.

Our domain, called Arctic and Northern Hemisphere Atlantic (ANHA), is a subdomain of the global ORCA12 domain. It covers the Arctic and the Northern Atlantic Oceans with a resolution of 1/12° (about 3.5 km in the CAA). In vertical, there are 50 levels with layer thickness increasing with depth from 1 m for the first level to 146 m at the 31st level (at a depth of 453 m). The bathymetry in the Arctic is derived from the 1 minute-arc global relief model of Earth's surface ETOPO1 (Amante & Eakins, 2009). Two open boundaries are present in the Bering Sea and at 20°S in the Atlantic Ocean, respectively. Open boundary conditions (temperature, salinity, and horizontal velocities) are obtained from the GLobal Ocean ReanalYSis 2 version 3 (GLORYS2v3 Masina et al., 2015). Surface forcing, that is, 10-m winds, 2-m temperature, and specific humidity, as well as surface downwelling shortwave and longwave radiative fluxes are taken from the high temporal and spatial resolution atmospheric forcing from the Canadian Meteorological Centre's Global Deterministic Prediction System ReForcasts (CGRF; Smith et al., 2014). The initial conditions (ocean temperature, salinity, horizontal velocities, and sea surface height) are taken from GLORYS2v3.

Runoff is based on the interannual monthly 1° × 1° river discharge data from Dai et al. (2009), as well as Greenland meltwater (5 km × 5 km) provided by Bamber et al. (2012). The source runoff is carefully (volume conserved) remapped onto the model grid. The river runoff data set ends in 2007, while the Greenland runoff goes up to 2010. At the end of each data set, the data from the last year is repeated until the end of the simulation.

Our numerical experiment starts from January 2002 and is integrated to the end of December 2016. If not stated otherwise, the results presented in this paper start from November 2003. This is done to consider model adjustment from the initial conditions. We define the winter months as the period from November to April of the following year and the summer months as the period from May to October. The sign convention for transport is defined as a positive value means toward the North Atlantic (i.e., Arctic outflow), while a negative value means into the Arctic Ocean. The reference salinity is chose to 34.8 in freshwater flux calculation.

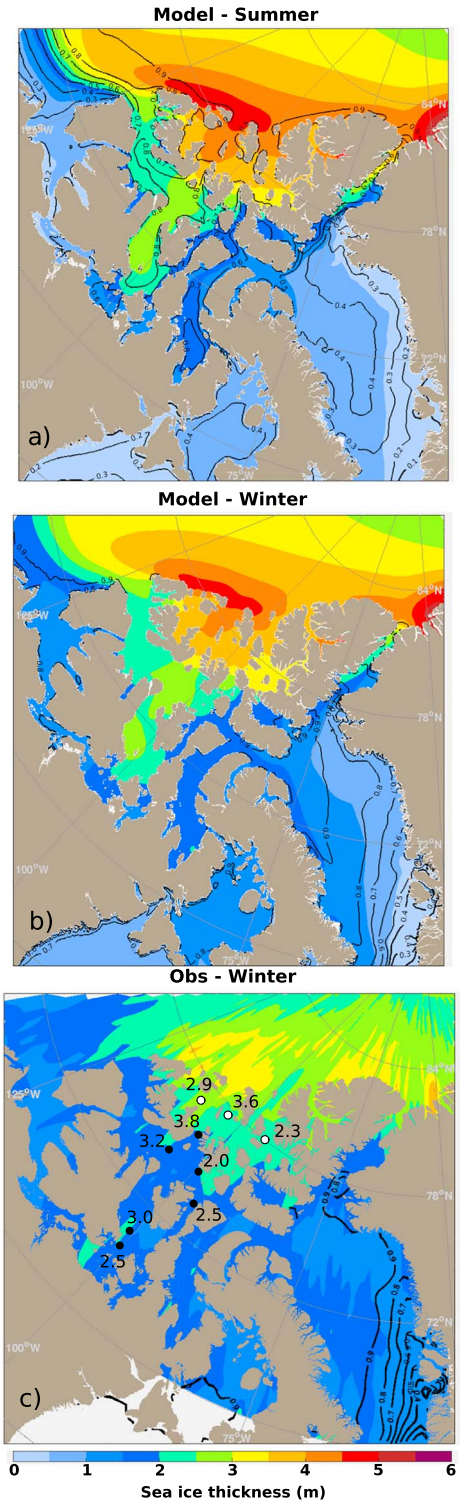

Figure 2. Sea ice thickness (shading) and concentration (contour lines) for summer (a) and winter (b) and observations for the winter period (c). Observations south of 66° N are masked. The black points are airborne electromagnetic measurements from Haas and Howell (2015) from late winter 2011 and 2015. White dots are drill hole measurements from Melling (2002) from late winter in the 1970s. Both are in meters.

2.2. Observations

2.2.1. Satellite Data

Sea ice concentration observations are based on the data from the Special Sensor Microwave/Imager (SSM/I) sensors on the Defense Meteorological Satellite Program's (DMSP)-F8, DMSP-F11, and DMSP-F13 and theScanning Multichannel Microwave Radiometer on the Nimbus-7 satellite. Measurements from the Special Sensor Microwave Imager/Sounder aboard DMSP-F17 are also included. The data set has been generated by using the Advanced Microwave Scanning Radiometer—Earth Observing System Bootstrap Algorithm with daily varying tie points (Comiso, 2000, updated 2015). We used the daily data averaged over the winter period from 2003 to 2016. The data are gridded on the SSM/I polar stereographic grid (25 × 25 km).

Sea ice thickness data are combined from the ICESat1-G (2003–2008) and CryoSat-AWI (2011–2017) data set extracted from the Unified Sea Ice Thickness Climate Data Record (Lindsay & Schweiger, 2013, updated 2017). ICESat1-G data are derived from measurements made by from the Ice, Cloud, and Land Elevation Satellite (ICESat) Geoscience Laser Altimeter System instrument, the SSM/I, and climatologies of snow and ice drift. CryoSat-AWI thickness is derived from Radar Altimeter freeboard measurements. Due to the irregularity in the position of each data point between the data set and within the years in the same data set, we averaged all data over 1° bins first, then over the winter period from 2003 to 2016. The years with no data available (2009–2010) have been ignored in the averaging. No sufficient observations are available in summer for a meaningful comparison and thus have been ignored.

2.2.2. Mooring Data

Two locations with moorings are available in the study region: at Nares Strait and West Lancaster Sound. At Nares Strait, observations are available for two periods, from August 2004 to August 2006 and from August 2007 to August 2009 (Münchow, 2016). The daily average of detided data is used here. More in depth description of the moorings is available in Münchow and Melling (2008). At West Lancaster Sound, observations are available from August 1998 to August 2010. Both monthly and 6-hourly detided data are used in this study. More details of the mooring data are available in Prinsenberg et al. (2009) and Peterson et al. (2012). In order to compute the correlation between model and observation, high frequency observations (either daily or 6-hourly) are averaged every 5 days (same frequency as model output).

3. Evaluation

3.1. Sea Ice

In summer (Figure 2a), ice concentration is 70% to 80% in the western and central Parry Channel and decreases gradually to 50% at the mount of Lancaster Sound. Spatial variation in ice concentration also exists in Peel Sound, high (~80%) on the west side and lower (~70%) on the east side. The Amundsen Gulf is almost ice free (less than 30%). Within Baffin Bay, the ice concentration is low on the Greenland side because of the intrusion of warm water carried by West Greenland Current at depth. In winter (Figure 2b), the CAA is fully covered by the sea ice, with the exception of the North Water Polynya where the sea ice concentration decreases slightly (~80%). The sea ice edge is located at the eastern part of Davis Strait over the Greenland continental shelf.

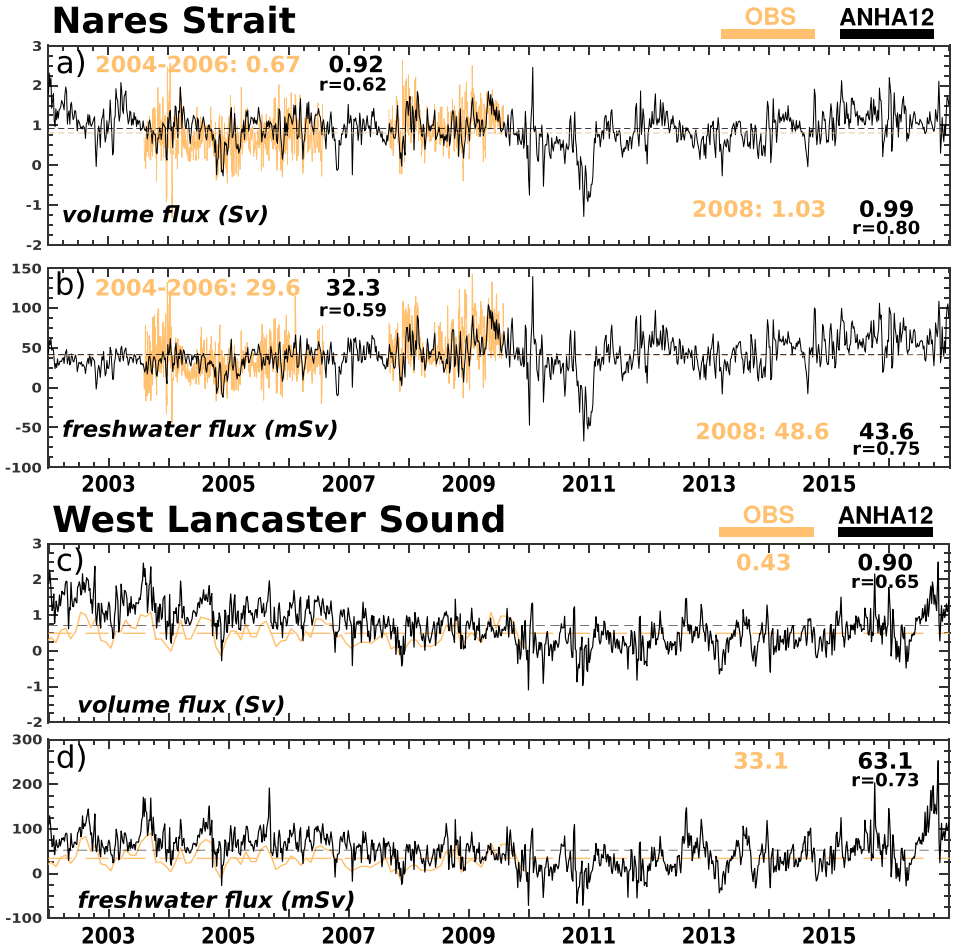

Figure 3. Observed (gray line) and simulated (black line) volume and freshwater transports for Nares Strait (a and b) and West Lancaster Sound (c and d). The average transports and correlations are computed over the common period of time between observations and model outputs. The dashed lines correspond to the average over the whole period for each time series plotted on the figure. ANHA = Arctic and Northern Hemisphere Antlantic.

In summer, sea ice thickness is up to 5.5 m around the Prince Patrick, Baden, and Ellef Ringnes Islands (Figure 2a). Ice thickness within the QEI is around 5 m while it is less than 1 m in Parry Channel and Amundsen Gulf. In winter (Figure 2b), ice thickness within Amundsen Gulf increases up to 2 m. The maximum sea ice thickness stays around 5.5 m. Sea ice distribution and thickness over the rest regions of the CAA does not change significantly. We note that the model forms thicker sea ice in summer in the QEI and Nares Strait. This is due to the summer and winter periods definition here. It is also evidenced in Hu et al. (2018) with a different definition (figure 4a and b in their paper).

Overall, sea ice concentration in winter in the model compares well with the available observations for the same period (Figure 2c). The main difference is the 90% sea ice concentration contour of the observation occurs further south. But this should not impact the analysis in this study. The overall spatial pattern of the sea ice thickness in the model matches the observations. The main difference is that the simulated sea ice is thicker than in the satellite data, especially in the QEI where the difference is about 1.5 m. Compared to the drill hole measurements in the late winter of 1970s (Melling, 2002), the simulated sea ice thickness is still thicker but with a smaller difference. In the Northwest Passage, simulated sea ice thickness, however, is very close (only ~0.5 m thicker) to observations from the airborne electromagnetic survey performed in late 2011 and 2015 (Haas & Howell, 2015). At Nares Strait, the simulated sea ice thickness is about 2 m, which agrees the winter observations from 2002 to 2012 that the median daily ice draft is from 1.5 to 3 m (Ryan &

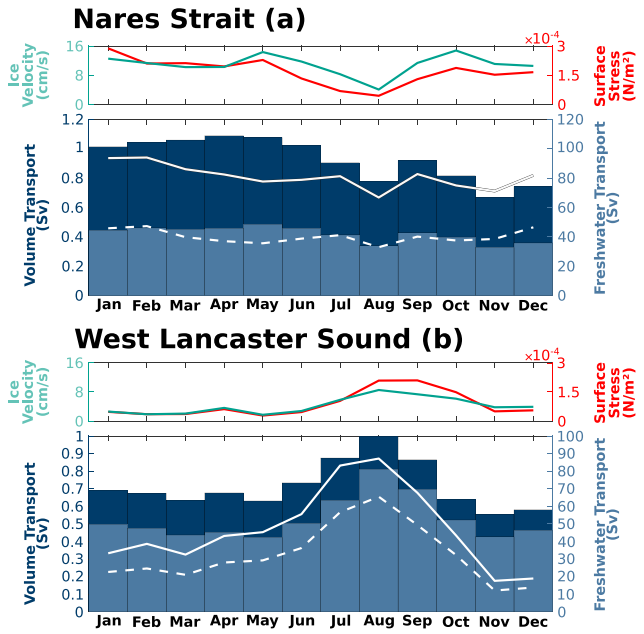

Figure 4. Seasonal cycle (bars) of the volume (dark blue) and freshwater (light blue) transports through Nares Strait (a) and West Lancaster Sound (b). White solid (dashed) line is the volume (freshwater) transport seasonal cycle from observations. Volume (freshwater) transport is associated with the left (right) axis. Each upper panel shows the ice velocity (green line, left axis) and surface stress (red line, right axis) directly above the section. Note that different scales are used for left-hand and right-hand *y* axes in each panel.

Münchow, 2017). A more complete analysis of sea ice thickness changes and dynamic-versus-thermodynamic contributions can be found in another study based on the same numerical experiment by Hu et al. (2018).

3.2. Transports via Nares Strait

The modeled volume transport at Nares Strait over the whole time period of 2002–2016 is 0.92 ± 0.44 Sv (Figures 3a and 3b). The interannual variability is relatively small or insignificant except in 2010. In 2010, the transport decreased significantly, even switched the direction in November (i.e., back to the Arctic Ocean).In the first common period (2004–2006), the modeled volume (freshwater) transport is 0.92 ± 0.36 Sv (32 ± 14 mSv), which compares well with the observed 0.67 ± 0.44 Sv (30 ± 21 mSv). The correlation between the observation and the model is $r = 0.62$ ($r = 0.59$). During the second common period (2007–2009), the simulated transport is 0.99 ± 0.37 Sv (freshwater transport: 44 ± 21 mSv), which compares well with the observed 1.03 ± 0.35 Sv (49 ± 22 mSv). The correlation between the model and observation is $r = 0.80$ ($r = 0.75$), which is higher than that in the first common period. We note that the correlation between volume and freshwater transports is greater than 0.95, which is consistent with observations (Münchow, 2016).

The seasonal cycle of the volume and freshwater transport is shown in Figure 4a. The seasonal cycle for the observations are computed from all available data, while the seasonal cycle for the model is computed from winter 2003 to summer 2016. It shows that the model has too much volume transport between March and June (i.e., during the end of winter) and not enough in November and December. The seasonal cycle for the freshwater transport is similar, except in December. In December, the model underestimates the freshwater transport more than what it does for the volume transport (Figure 4a; ~10 mSv less than observations).

3.3. Transport via West Lancaster Sound

At West Lancaster Sound, the average modeled volume (freshwater) transport for the whole time period is 0.71 ± 0.55 Sv (53 ± 38 mSv). Over the common period (2002 to 2010), it is even larger, 0.95 ± 0.52 Sv (63 ± 33 mSv), compared with observations, 0.46 ± 0.56 Sv (32 ± 24 mSv; Figures 3b and 3d). The correlation between the model and observations is $r = 0.65$ ($r = 0.73$). The seasonal cycles shows that the transport in the summer months in the model is close to observations (Figure 4b). However, the volume transport during the winter is 75% higher than observations (about 0.7 Sv instead of 0.4 Sv). The modeled freshwater transport is slightly better, only 55% higher than the observation (about 45 vs. 20 mSv).

Using high-resolution observations, we expand the fluxes analysis for each subsection across the West Lancaster Sound (Figure 5). For the details about how the observations are computed per subsection, please see Peterson et al. (2012) and Prinsenberg et al. (2009). The model mean transport is slightly higher than observations between 2002 and 2009 in the southern part, but it is close to the observations in the other parts and after 2009. The transport through the south section decreases progressively, being more comparable with the observations. The variability is satisfyingly represented by the model for each subsection (Figure 5). Several cells are used in the model to compute the transports, while only one mooring is available for each subsection; thus, uncertainty in observation is not considered here.

Overall, the model represents the observed transport relatively well. The model overestimates both volume and freshwater transport for each section for the early years but becomes close to observation both in mean value and correlation in later years. The reasons behind the overestimates on the transports is discussed in section 4.1. More evaluation on the transport through the CAA, including current velocity and surface density, and mixing processes in this region is described by Hughes et al. (2017) for a similar experiment.

3.4. Transport via the Other Major Gates in the CAA

An overall picture of the oceanic transports through the CAA are shown in Figures 6a and 6b for volume and freshwater transport, respectively. A summary is shown in Table 1 as well as values from other studies. We

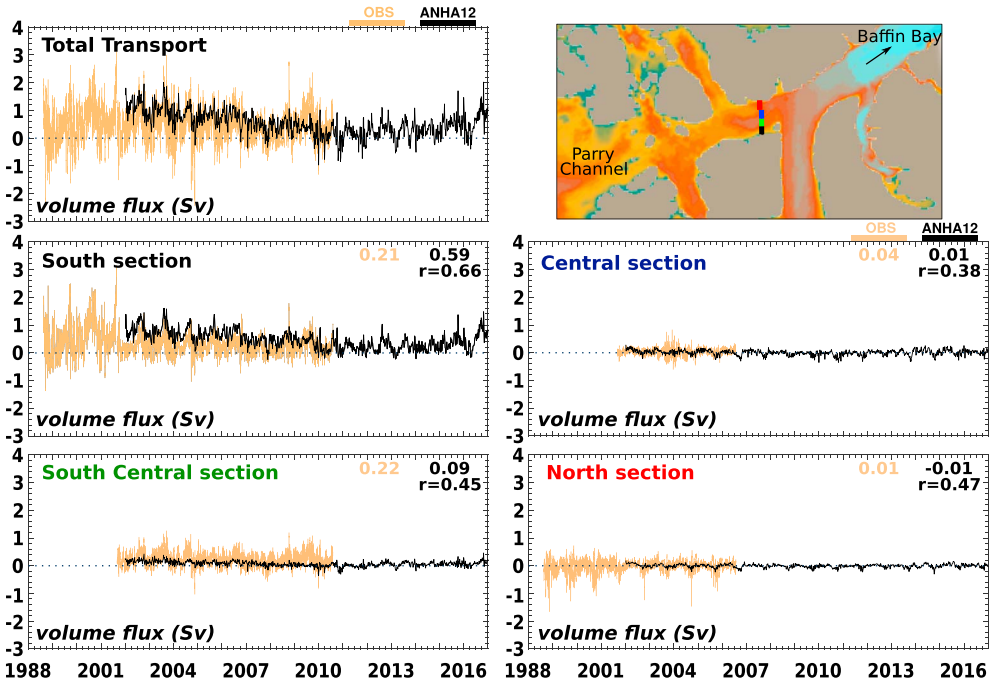

Figure 5. Volume transport (orange line: observation; black line: model) through each individual subsection along Barrow Strait observation section. The total transport is shown in the top left panel. Location of each subsection is shown in the top right panel. The other panels represent the transport through each subsection. The line colors of each subsection in the top right panel correspond to the color in the name of each subsection in the transport panels. ANHA = Arctic and Northern Hemisphere Atlantic.

note that the transport values from the 1980s and earlier are computed based on only a few observations. The modeled volume (freshwater) transport going into the QEI from the Arctic Ocean is about 0.16 Sv (8 mSv), which is about 40% (30%) of the incoming transport through M'Clure Strait (0.40 Sv; 27 mSv). Part of the inflow through M'Clure Strait could enter the QEI via the strait between Prince Patrick Island and Melville Island. It is 0.05 Sv (4 mSv) in our simulation. However, whether it is a realistic case or a bias due to model resolution needs further investigation.

This suggest this region is important in terms of exchanges through the CAA. Eighty percent of the QEI inflow enters Parry Channel via Byam Martin Channel (0.17 Sv for modeled volume and 0.03 mSv for modeled freshwater transport) and 15% via Penny Strait and Wellington Channel (0.03 Sv for modeled volume and 1 mSv for modeled freshwater transport). Jones Sound has a negligible effect on the volume and freshwater outflow out of the QEI in the simulation. These values compare well with a previous numerical experiment from Wekerle et al. (2013) who obtained modeled volume (freshwater) transports of 0.45 Sv (40 mSv), 0.27 Sv (22 mSv), and 0.09 Sv (7 mSv) through M'Clure Strait, Byam Martin Channel, and Penny Strait, respectively. Only the modeled freshwater flow via M'Clure Strait is significantly higher in our experiment, while the simulated flow through Jones Sound is significantly lower than the one obtained by Zhang et al. (2016), which also has a significantly higher simulated flow at Lancaster Sound compared with observations. The modeled volume transport is stronger in the western part of the QEI (~80% of the transport follows this route), and a weak eastern simulated flow is present inside of the QEI between the western and eastern part (0.01 Sv; 1 mSv).

Amundsen Gulf receives about 0.05 Sv (4 mSv) from the Arctic Ocean. This inflow later enters Parry Channel via Prince of Wales Strait due to the high sea surface height (SSH) in Coronation Gulf. Compared to a previous numerical study by Wekerle et al. (2013), the volume flux through this pathway is 5 times larger in our simulation. The difference could be due to difference in model resolution in this region. We also note that the direction of freshwater transport in our simulation is different than in Wekerle et al. (2013) due to a difference in the sign of the volume transport.

The simulated flow in the central Parry Channel goes around the Prince of Wales Island via the M'Clintock Channel and Peel Sound, which agrees with previous studies (Wang et al., 2012; Wekerle et al., 2013; Zhang

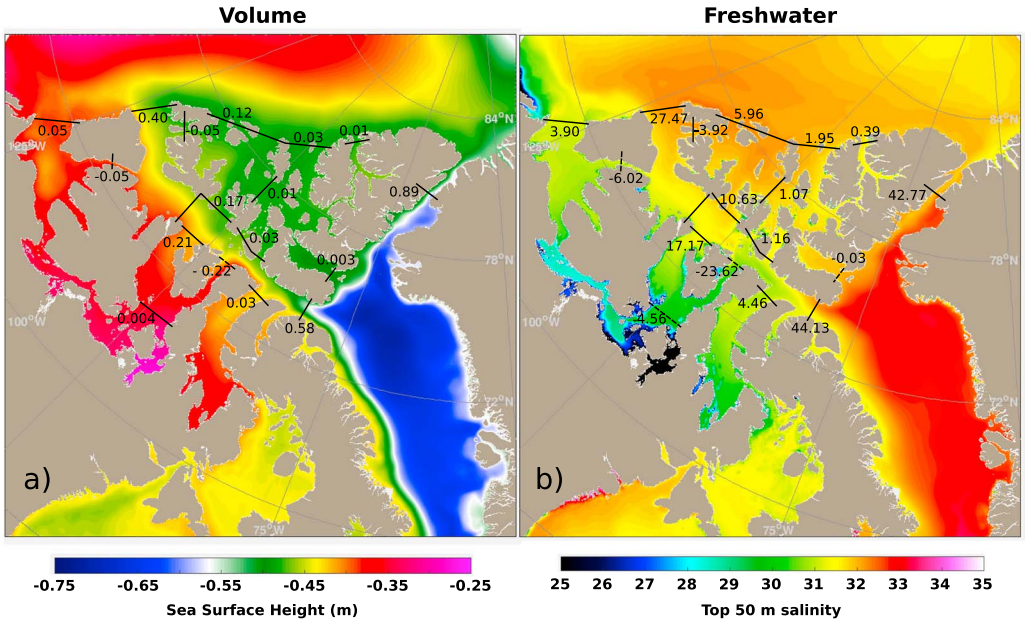

Figure 6. Sea surface height (a) and top 50-m salinity (b) in the Canadian Arctic Archipelago. The numbers represent the volume (a, unit: Sv) and the freshwater transport (b, unit: mSv) through the Canadian Arctic Archipelago averaged from November 2003 to December 2016. Transport is positive when going toward the North Atlantic and negative when going toward the Arctic Ocean.

et al., 2016). The modeled transport through M'Clintock Channel and Peel Sound is 0.21 Sv (17 mSv) and 0.22 Sv (24 mSv), respectively. These numbers compare well with Wekerle et al. (2013), 0.27 Sv (24 mSv) and 0.29 Sv (26 mSv), respectively.

The increase in transport through Peel Sound is from Victoria Strait (~0.01 Sv). Due to low salinity (<20) in its upstream region, the freshwater transport can be as large as 5 mSv, which represents about one fifth of the freshwater flow through Peel Sound. This indicates a nonnegligible freshwater source into Parry Channel.

4. Surface Stress and Ice Velocity

4.1. West Lancaster Sound and Nares Strait

The difference in quality of the simulated volume and freshwater transports at West Lancaster Sound and Nares Strait can be explained by the different impact of the ice velocity on the transport.

It is found the simulated volume transport is high correlated to surface stress both at West Lancaster Sound ($r = 0.75$) and Nares Strait ($r = 0.53$). The variation of surface stress at West Lancaster Sound is mainly controlled by ice velocity with a correlation of 0.96, which indicates the variation of the transport here is due to ice motion. At Nares Strait, the correlation between surface stress and ice velocity is lower ($r = 0.72$), suggesting a bigger role from the wind. Similarly, difference in surface stress sources may also play a role in the freshwater transport. The modeled freshwater transport is highly correlated to the surface stress at West Lancaster Sound ($r = 0.90$), while $r = 0.55$ at Nares Strait.

The timing of the overestimated transport through the two straits is found to be correlated to the too-mobile ice in the simulation. Figure 4b shows larger discrepancies between observation and simulated volume transport occur in the winter months, that is, November to May in the following year. During this period, the simulated mean ice velocity is as large as 3 cm/s, leading to too big downstream flow. Similarly at Nares Strait, the fast ice motion (up to 14 cm/s in May) in April–June results in the largest overestimating in the volume transport in our simulation. At Nares Strait, Ryan and Münchow (2017) showed the landfast ice exists in May of most years between 2003 and 2012 based on observations. The sea ice jam is also an important physical process that controls the sea ice dynamics at Nares Strait. However, the model utilized here does not resolve landfast ice physics, for example, using the parameterization from Lemieux et al. (2016). Therefore, the modeled sea ice velocity is usually higher compared to the real word. The ice bridge is not resolved either; however,

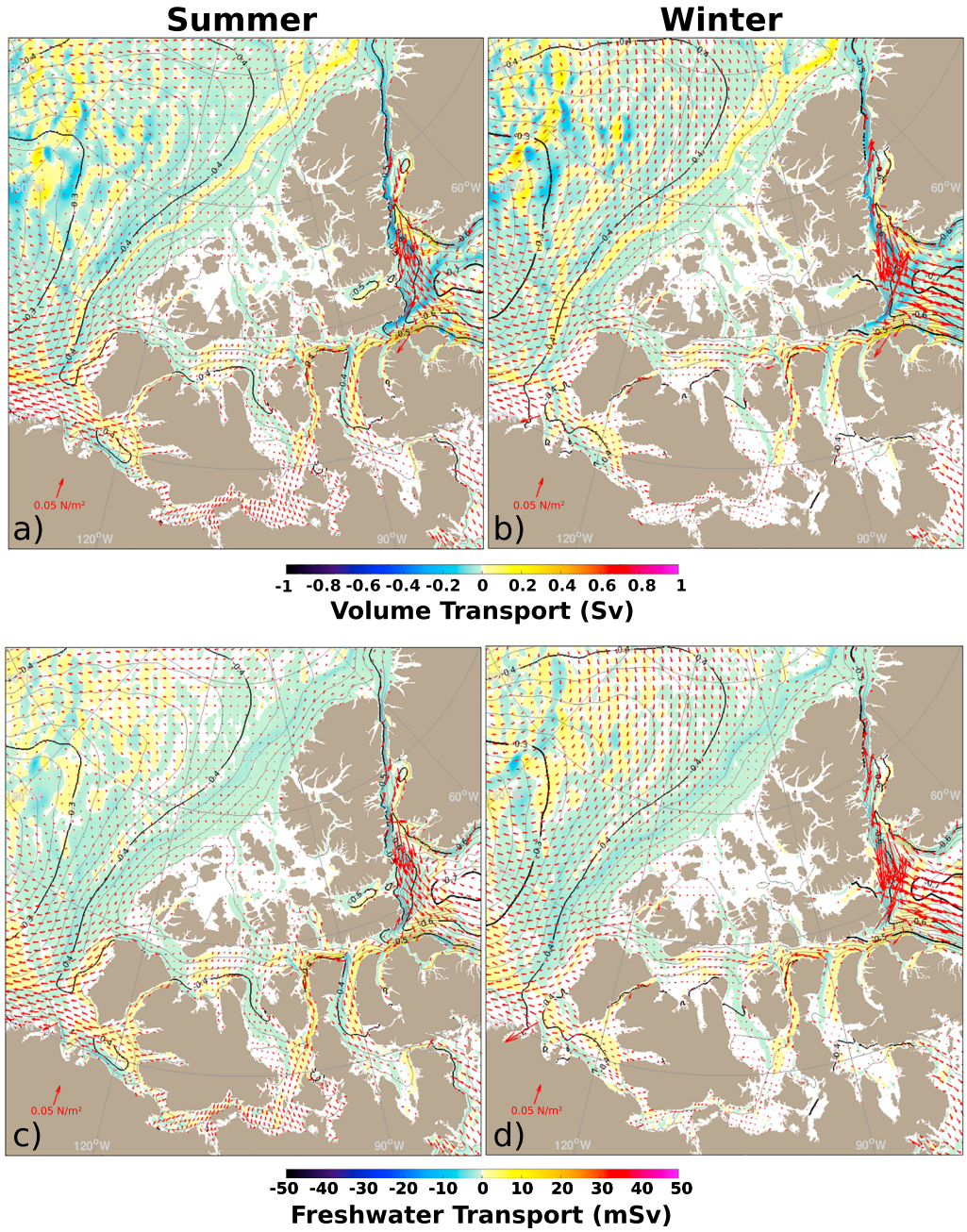

Figure 7. Maps showing the volume (a and b) and freshwater (c and d) transports at each point of domain (shading) whith the surface stress (arrows) and sea surface height (black contour lines) averaged over all summers from 2004 to 2016 (a and c) and all winters from 2003 to 2016 (b and d).

the accumulation of ice in the narrow channel plays a similar but limited role to reduce the ice velocity (see Figure 4d in Hu et al., 2018). It explains why the transport overestimation at Nares Strait happens later than that at West Lancaster Sound in our simulation.

Although too-mobile sea ice leads to overestimated transport through both West Lancaster Sound and Nares Strait, the role of sea ice is different. At West Lancaster Sound, the surface stress (same for the ice stress, not shown here) is in opposite direction of the surface flow (Figure 7b); thus, the ice works as a drag reducing the ocean flow. As the ice is too mobile, the reduction of ocean flow due to surface stress is not enough, resulting in larger volume transport to downstream. However, at Narest Strait, the ice is drifting faster than the ocean surface flow (not shown); thus, the surface stress is in the same direction as the ocean flow (Figure 7b).

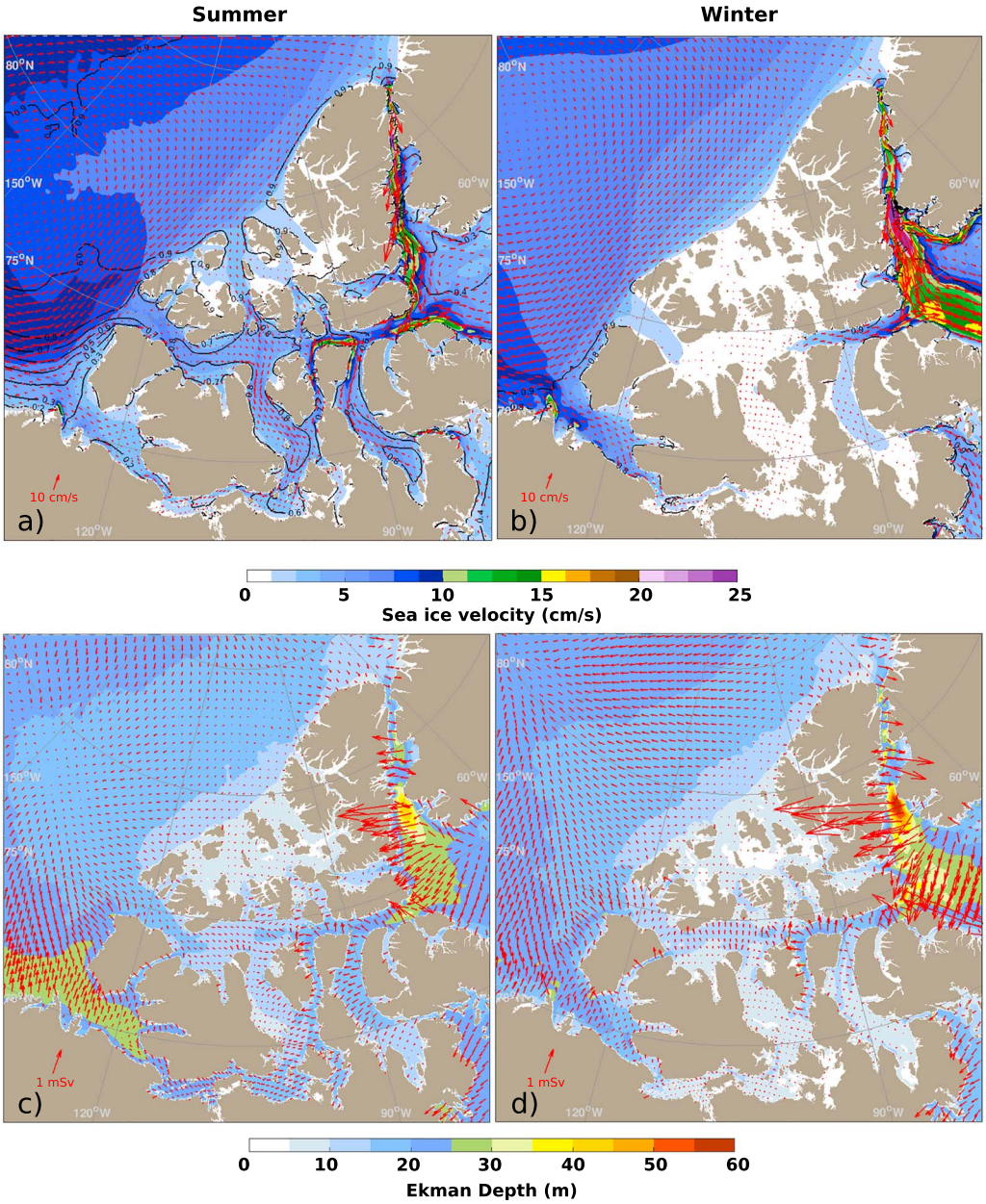

Figure 8. The top panels show the sea ice velocity (shading) and direction (arrows) for summer (a) and winter (b). The bottom panels show the Ekman Depth (shading) and Ekman Transport (arrows) for summer (c) and winter (d).

Therefore, sea ice there does drive a faster surface ocean current. Different ice-ocean interactions are likely due to much stronger along channel wind at Nares Strait. More discussion about the dependence of Nares Strait oceanic transport on the sea ice motion is available in Shroyer et al. (2015).

4.2. Other Straits Over the CAA

In summer (Figure 8a), sea ice velocity in the numerical experiment is small in most of the CAA with a velocity less than 1 cm/s in the QEI, except in the main channels where the velocity can be up to 3 cm/s. In the southern CAA, this velocity increases up to 7 cm/s. High sea ice velocity (up to 16 cm/s) can be found at Barrow Strait, at the mouth of Lancaster Sound, in Nares Strait, and in the area of the North Water Polynya. In winter (Figure 8b), despite not having real landfast ice in the model, the ice velocity is less than 1 cm/s over most of the CAA. High velocity (up to 10 cm/s) can be found in the Amundsen Gulf and in Lancaster Sound in the numerical experiment. Much larger (more than 25 cm/s locally) ice velocity is seen along the path from Nares Strait to

Figure 9. Correlation between the surface stress and the volume transport in summer for the sections defined by the thick black line in each panel. All values with a confidence level lower than 0.05 have been masked out. The black boxes in the top left figure (a) show the boxes used to define the remote correlations in Table 2. CAA = Canadian Arctic Archipelago; QEI = Queen Elizabeth Islands.

eastern Baffin Island coast. Observations (Ryan & Münchow, 2017) also shows large velocity in this region but with a lower winter average velocity due to the presence of ice bridge.

Another way to quantify the impact of surface stress on the ocean flow is Ekman depth and Ekman transport (Appendix C). Figures 8c and 8d show the summer and winter Ekman depth (colors) and transport (arrows) in the CAA region based on model simulation. It clearly shows Ekman depth is deeper in summer (Figure 8c) in most regions of the CAA (QEI, Amundsen Gulf, and south CAA). The Ekman depth shallowing is associated with a 50% decrease of surface stress in these regions in winter (Figure 8d), indicating weaker transport there.

Table 2
Relative Strength of the Local and Large-Scale Correlation for Each Strait Shown in Figure 9

		Summer		Winter	
Panel	Section name	Local	Large	Local	Large
(a)	Ballantyne + Price Gustaf Adolf Strait	$Weak^{+}$	None	$Weak^{-/+}$	$Weak^{-/+}$
(b)	Ellef Ringnes – Axel Heiberg Island Strait	$Weak^{\tau/-}$	$Strong^{-/-}$	$Weak^{-}$	$Weak^{-/\tau}$
(c)	Central QEI	$Weak^{+/-}$	$Weak^{-/-}$	$Weak^{-}$	None
(d)	Prince Patrick Island – Melville Island Strait	$Weak^{-}$	$Weak^{+/+}$	$Strong^{-}$	$Weak^{+/-}$
(e)	Byam Martin Channel	$Weak^{+}$	$Weak^{-/\tau}$	$Strong^{+}$	None
(f)	Penny Strait + Wellington Channel	$Weak^{-}$	$Strong^{-/\tau}$	$Strong^{-/+}$	$Weak^{-/-}$
(g)	Lancaster Sound	$Weak^{+/-}$	$Strong^{-/\tau}$	$Strong^{+}$	$Weak^{-/\tau}$
(h)	M'Clure Strait	$Weak^{-/\tau}$	$Weak^{-/\tau}$	$Weak^{+/-}$	$Weak^{-/\tau}$
(i)	Prince of Wales Strait	$Weak^{+/-}$	$Strong^{+/\tau}$	Strong-	$Weak^{+/\tau}$
(j)	Mc Clintock Channel	Weak+	$Weak^{-/\tau}$	Strong+	$Weak^{-/\tau}$
(k)	Peel Sound	$Weak^{-}$	$Weak^{+/\tau}$	$Strong^{-}$	$Weak^{+/\tau}$
(l)	Gulf of Boothia	$Weak^{+}$	$Weak^{\tau/+}$	$Weak^{+}$	$Weak^{\tau/+}$
(m)	Amundsen Gulf	$Strong^{-}$	$Strong^{-/-}$	$Strong^{-}$	$Strong^{-/\tau}$
(n)	Victoria Strait	$Weak^{-}$	$Strong^{-/-}$	$Weak^{+}$	$Weak^{-/\tau}$
(o)	Jones Sound	$Weak^{-}$	$Strong^{-/-}$	None	$Weak^{-/-}$
(p)	Nares Strait	$Weak^{+}$	$Weak^{\tau/+}$	$Strong^{+}$	$Weak^{\tau/+}$

Note. The superscript in the Local columns indicates the direction of the correlation (+: positive correlation; –: negative correlation; both means that both correlations are present). The superscript in the Large columns indicates the correlation over the Beaufort Gyre (first superscript) and over the northern Baffin Bay (second superscript). The superscript ø indicates when there is no significant correlation over the considered region.

However, it is a different case in the eastern part of the CAA and Baffin Bay. At Nares Strait, the Ekman depth is deeper in winter by up to 70% due to an increase of the surface stress over the strait. In the following section, we will focus on how and from where the transport through the CAA is affected by the surface stress.

4.3. Correlation Between Volume Transport Through Main Gateways and Surface Stress in Space

To better understand the impact of surface stress on ocean transports, we correlated the transport (volume and freshwater, respectively) time series via main gateways in the CAA with surface stress time series at each model individual point. To remove the linear adjustment of the model, both time series are linearly detrended (more information on how and why the correlation is computed this way is provided in Appendix D). The correlation is performed for summer and winter periods separately. A positive correlation means that a stronger surface stress enhances the mean transport, while a negative correlation means a stronger surface stress weakens the mean transport. The spatial distribution of correlation can be interpreted in two aspects. A significant correlation close to the section means that the variability in the transport can be explained by local or immediate upstream/downstream changes in the surface stress forcing (i.e., the atmospheric forcing or the sea ice motion, depending on the sea ice cover). A significant correlation farther away from the section shows how much of the variability can be explained by remote changes in the surface stress. In the second case, we define two regions of interest: over the Beaufort Gyre and in northern Baffin Bay, shown in Figure 9a. The strength of the correlation is classified as *none* ($r \leq 0.1$ or not significant at a significance level of 0.05), *weak* ($0.1 < r < 0.5$), and *strong* ($r \geq 0.5$). A summary of the relative strength of each aspect for each section is shown in Table 2. We note that this method does not take into consideration the change in direction of the surface stress. However, the direction of the surface stress does not show any significant changes along the course of our experiment that could significantly impact our results (not shown).

Overall, in summer (Figures 9b and 9c), it shows a local negative correlation between the surface stress and the transport in most of the QEI, indicating that the surface stress tends to reduce the transport across the CAA and from the west to the east of the QEI. The exceptions are the Ballantyne and Prince Gustaf Adolf straits (Figure 9a) where the correlation is mainly positive downstream and upstream in the northern part of the strait only. A local negative correlation is also present west of Baden Island.

The flow toward Parry Channel (Figures 9e, 9i, 9j, and 9l) and Nares Strait (Figure 9p) have a positive local correlation, with the exception of M'Clure Strait (Figure 9h), Prince Patrick Island – Melville Island Strait (Figure 9d), Peel Sound (Figure 9k), and Penny Strait (Figure 9f). Flow through M'Clure Strait shows only a negative correlation with upstream surface stress but no significant correlation with downstream stress. Similarly, negative correlation with local stress is found in Penny Strait but no significant correlation in the downstream (Wellington Channel). Flow through West Lancaster Sound is found to be positively correlated to upstream stress and negatively correlated to downstream stress within Parry Channel. Negative correlation with local surface stress is found in Amundsen Gulf (Figure 9m) and Victoria Strait (Figure 9n).

The local negative correlation in the northern QEI, in the southern CAA, and at M'Clure Strait can be explained by the direction of the mean surface stress over the CAA (Figure 7a). The mean surface stress over the northern QEI is westward because the sea ice inside of the CAA is packed and has limited mobility. Consequently, the sea ice flows southward following the mean current. The Ekman transport associated with this motion is directed outside of the CAA (Figure 8). This is well shown in the central QEI (Figure 9c). The baroclinic gradient however is in the opposite direction, pushing the water into the CAA, such as shown by the volume transport (Figure 6a). The surface stress is thus in the opposite direction of the mean flow. A reduction of the stress will thus increase the flow through the section (less Ekman transport in the opposite direction).

For Parry Channel, the correlations can be explained by the sea ice concentration (Figure 6a) and motion (Figure 6c). The straits toward Parry Channel have relatively lower sea ice concentration and the higher sea ice motion (~5 cm/s) compared with the other straits in the CAA. The ice is thus flowing southward toward Parry Channel, leading to the mean flow and Ekman transport to be almost in the same direction. Thus, the surface stress tends to accelerate the flow. At M'Clure Strait, the mean ice motion is along the edge of the CAA coastline. An increase in the surface stress tends to move the ice outside of Parry Channel and the Ekman transport pushes the flow outside of the CAA. Inside of Parry Channel, the geometry of the straits that controls how ice motion will impact the Ekman transport. At Byam Martin Channel, the opening is relatively large, letting the ice flow to the south. An increase of stress drives more ice and more transport. At Penny Strait and Wellington Channel, an increase of surface stress jams the ice inside of Parry Channel and thus reduces the transport.

West Lancaster Sound is a peculiar case because the flows through this strait are not unidirectional in summer, as shown previously. Consequently, surface stress acting upstream will accelerate the flow due to the Ekman Transport, while downstream stress will accelerate the northward flow (i.e., positive correlation), which reduces the mean southward transport as the stress increases (i.e., negative correlation).

On the large scale, changes over the Beaufort Gyre and northern Baffin Bay are opposed to the changes in the transports over the QEI, with a strong negative correlation at the gates of the QEI from the Arctic Ocean and Lancaster Sound directly toward Baffin Bay. The changes in the surface stress over northern Baffin Bay do not significantly impact the transport. Over the Beaufort Gyre, the sign of the correlation can be explained by the dynamic of the Beaufort Gyre.

SSH in Beaufort Gyre is associated with the accumulation of mass caused by Ekman transport. A decrease in surface stress in this region will decrease Beaufort Gyre SSH and then flatten the baroclinic gradient between the Gyre and Baffin Bay, driving less transport through the CAA straits (e.g., Manucharyan & Spall, 2016; Manucharyan et al., 2016). The transports through Prince of Wales Strait (Figure 9i) and the strait between Prince Patrick and Melville Islands (Figure 9d) are positively correlated to surface stress in Beaufort Gyre. But the flows are not impacted by surface stress in Baffin Bay. We note that changes over Baffin Bay are related to the transport only for the strait between Prince Patrick and Melville Islands (Figure 9d).

There are three regions where the throughflow is not correlated to surface stress over the Beaufort Gyre. Flow through the Bellantyne and Prince Gustaf Adolf Straits is only correlated to local stress (Figure 9a). Transport through Nares Strait (Figure 9p) and the Gulf of Boothia (Figure 9l) show positive correlation with local and downstream (northern Baffin Bay) surface stress only.

In winter (Figure 10), the transport is impacted by the surface stress over a larger area for most of the straits. This can be explained by a more compact ice concentration moving more uniformly. Moreover, the correlation is usually stronger showing that the surface stress has a greater importance on the total volume transport in winter (e.g., Nares Strait, M'Clintock Channel, around Peel Sound). This suggests that sea ice concentration plays a stronger role in the control of transport variability than the wind in summer, which is consistent with

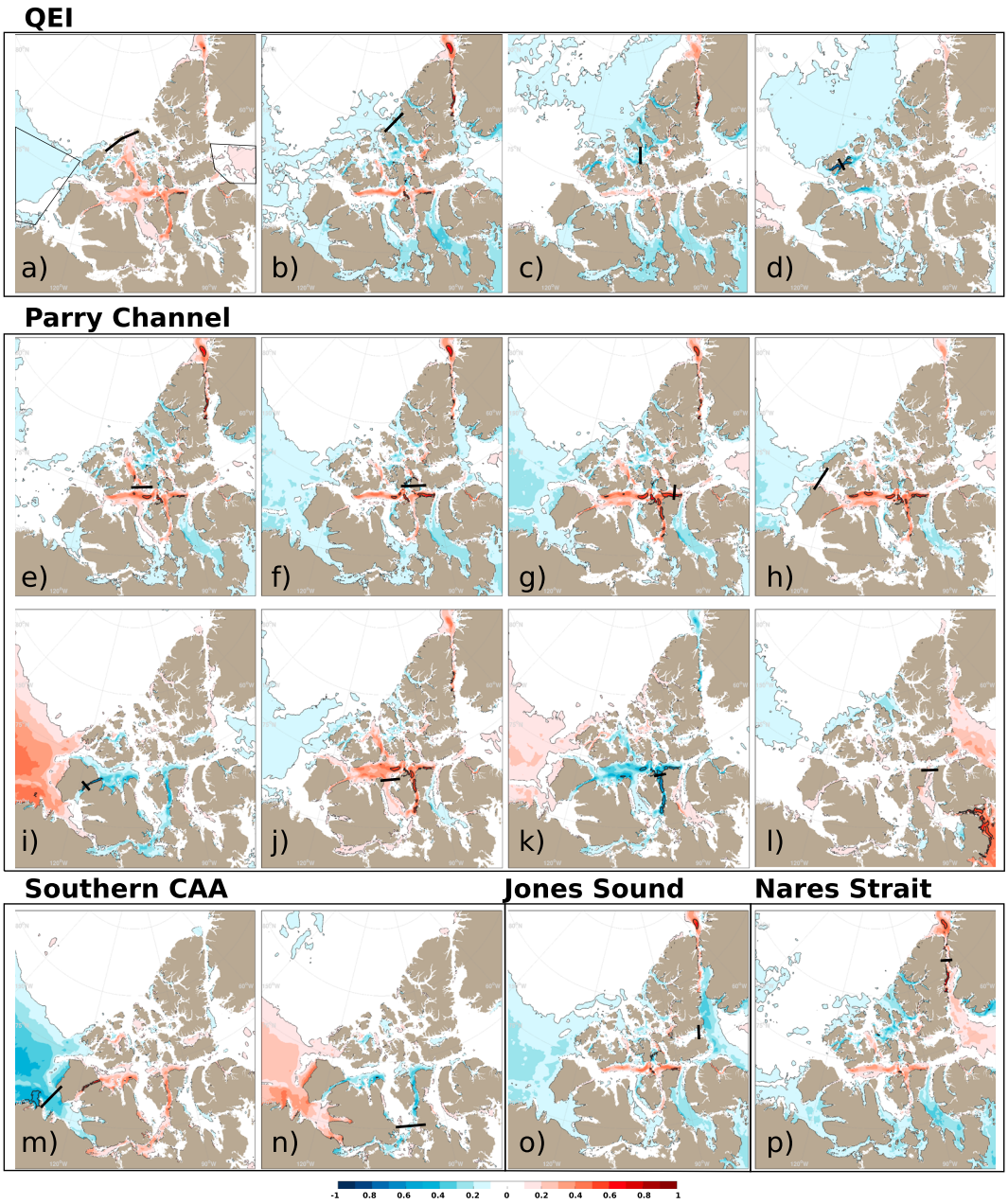

Figure 10. Same as figure 9 but averaged over winters from 2003 to 2016. CAA = Canadian Arctic Archipelago; QEI = Queen Elizabeth Islands.

a larger transport. We note that, for Nares Strait, these results are consistent with Münchow (2016) who also noticed a larger yearly volume transport when the sea ice is mobile throughout the year and lower when a sea ice bridge is formed in winter.

The dynamics are modified by the sea ice motion in several straits. At Prince of Wales Strait (Figure 10i) the correlation becomes strongly negative, showing that sea ice decreases the volume transport. This can be explained by the fact that the sea ice motion decreases along the strait, nearing 0 in Parry Channel.

At Byam Martin Channel (Figure 10e) the correlation is now strongly positive showing that, in winter, sea ice motion increases the volume transport. At Penny Strait (Figure 10f), the correlation is still negative, while it becomes positive at Wellington Channel (Figure 10f). The increase in sea ice velocity east of Barrow Strait permits the sea ice to flow more freely out of the QEI, thus leading to an increase in the transport.

At Jones Sound (Figure 10o), sea ice cover tends to reduce the correlation just at the strait, but the correlation increases in Norwegian Bay. This shows that the dynamics of Jones Sound in winter is not only related to the flow in northern Baffin Bay but is also related to the inflow from the QEI. At M'Clure Strait (Figure 10h) the correlation is still negative upstream but becomes positive over the western part of the strait, showing that sea ice motion over this region increases the incoming transport in Parry Channel but only in winter. At the entrance of the Gulf of Boothia (Figure 10l), the correlation becomes very localized showing that sea ice does not significantly impact the volume transport in winter. At West Lancaster Sound (Figure 10g), the absence of a bidirectional flow modifies the correlation to be only strongly positive: The flow is only impacted by sea ice motion upstream. Finally, at Victoria Strait (Figure 10n) the correlation is the opposite compared to summer showing that sea ice is increasing the volume transport.

4.4. Impacts on the Seasonal Freshwater Transport

Correlation between freshwater transports and surface stress is similar to the case of volume transport both for summer (Figure 11) and winter (Figure 12) through most straits in the CAA region. Different from the case of volume transport, freshwater transport is usually correlated to surface stress with a larger coefficient and over a larger area. This is due to the fact that freshwater transport is mainly occurring in the upper layer, which is more influenced by the Ekman transport.

However, the dynamics at some straits have changed. In summer, the correlations at Penny Strait and Wellington Channel become positive (Figure 11f), while at M'Clure Strait the correlation becomes positive only in the western part of the strait (Figure 11h). At Nares Strait, the positive correlation becomes more significant along the strait (Figure 11p). This shows that a weak variation in the surface stress might not impact the total transport but the freshwater transport will respond. This is true for the straits where the volume transport is relatively low, compared to the freshwater transport.

In winter, we notice fewer differences in the correlation between the volume and freshwater. The main difference is present at Jones Sound where the correlation is now locally positive (Figure 12o). This suggests that sea ice motion impacts the freshwater transport at Jones Sound in a similar way to what happens at West Lancaster Sound and Nares Strait (section 4.1).

The positive correlation in western M'Clure Strait is also significantly stronger for the freshwater transport (Figure 10h) than for the volume transport (Figure 12h). This shows that the sea ice motion at the entrance of Parry Channel could directly impact the freshwater inflow to the CAA even if the volume transport does not significantly change.

5. Conclusion

We analyzed the relative importance of each gate in the CAA for the volume and freshwater transport based upon a high-resolution numerical simulation. The transport across the QEI is about 40% of the transport entering Parry Channel at M'Clure Strait, mainly going through the western part of the QEI. The transports going through Amundsen Gulf represents less than 10% of the total inflow. We also showed the importance of Victoria Strait in the freshwater inflow into Peel Sound.

Detailed comparison with observations have been carried out. At West Lancaster Sound we compared observations from Peterson et al. (2012) with the model. The model overestimates the transport in winter, while the transports in summer are close to observations. At Nares Strait, we compared the model with observations from Münchow (2016). The model represents the transport during the winter and summer well but is too large during the melting and freezing seasons. In both cases this is due to too-mobile sea ice in the model but with different physical processes, sea ice drives more flow at Nares Strait while sea ice causes less reduction in transport at West Lancaster Sound. Similar relation is found between sea ice transport (surface stress) and freshwater transport with even higher correlation because freshwater transport is more dominated by surface waters.

We then explored the importance of the surface stress on the volume and freshwater transports at the main straits of the CAA in summer and winter. We show the different impacts on the transport: In the QEI the surface stress tends to act in the opposite direction of the transport, while in Parry Channel and in the southern part of the CAA the surface stress tends to enhance the oceanic transport. It is found that large-scale changes in the surface stress impacts each strait differently, with the QEI being more sensitive to changes over the Beaufort

Figure 11. Same as figure 9 but for freshwater transport. CAA = Canadian Arctic Archipelago; QEI = Queen Elizabeth Islands.

Gyre and northern Baffin Bay than the straits toward Parry Channel and the southern CAA. We also found the importance of sea ice motion in the transport with a high correlation between the transport and the surface stress in most of the CAA straits. When covered by sea ice, the local stress becomes more dominant in the transport, mainly over the regions with moving sea ice. For a few straits (e.g., Barrow Strait, Prince of Wales Strait, and M'Clure Strait) the presence of sea ice changes the correlation to enhance the transport instead of being opposed to it.

As a consequence of these findings, it raise the question, what will the future throughflow be? If the current downward trend in the sea ice over the CAA continues (e.g., Howell et al., 2009, 2013; Melling, 2002; Sou & Flato, 2009; Stroeve et al., 2007) the CAA will be almost sea ice free by 2050 (Hu & Myers, 2014). The transition will be slow, with more mobile sea ice in winter, especially in the QEI. The dynamic shown during

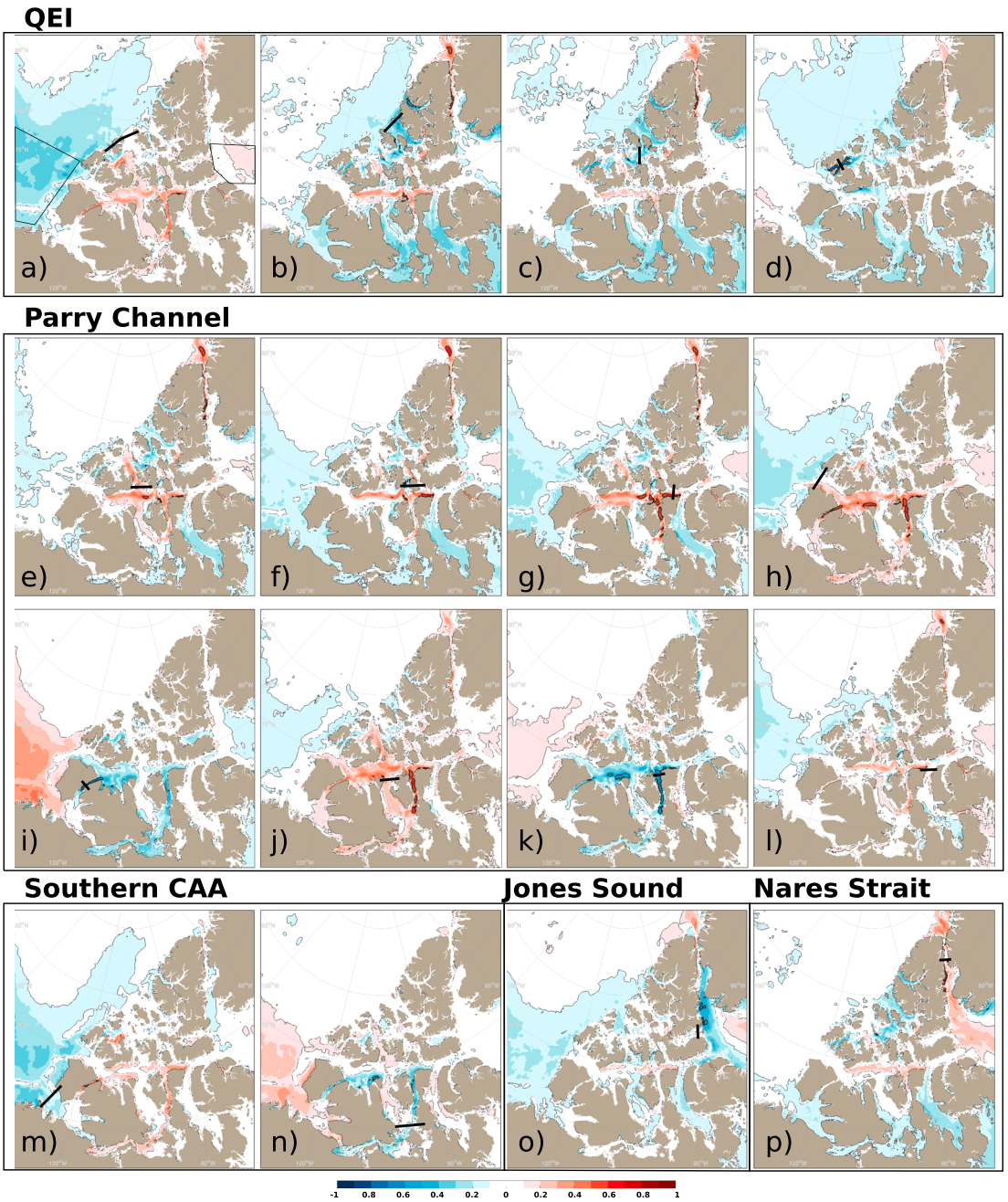

Figure 12. Same as figure 10 but for freshwater transport. CAA = Canadian Arctic Archipelago; QEI = Queen Elizabeth Islands.

the summer months in current paper will last over a longer time period and the surface stress will increase in winter, due to an increase in sea ice mobility, leading to more transport, even in winter. Consequently, the variability of the transport will be larger and depend more on the year-round atmospheric circulation.

Appendix A: Transports

The volume and freshwater transports are computed from 5-day averaged output from the numerical model as follows:

$$T_{\mathrm{Vol}} = \int_{H}^{0} v \, dA dz \tag{A1}$$

$$T_{FW} = \int_H^0 v \left(\frac{S_{ref} - S}{S_{ref}} \right) dA dz \tag{A2}$$

where H, v, dA, S_{ref}, and S are integration depth, the velocity normal to the section, the area of the section, the reference salinity ($S_{ref} = 34.8$), and the salinity, respectively.

Appendix B: Surface Stress

The total surface stress is defined as

$$\tau = (1 - i_c)\tau_{wo} + i_c \tau_{io}, \tag{B1}$$

where i_c, τ_{io}, and τ_{wo} are the ice concentration, surface stress due to the ice, and surface stress due to the wind, respectively. Surface stresses are computed with the bulk formulae:

$$\tau_{wo} = \rho_a C_{Do} \| u_w \| (u_w), \tag{B2}$$

$$\tau_{io} = \rho_o C_{Di} \| u_i - u_o \| (u_i - u_o), \tag{B3}$$

where ρ_a, C_{Do}, C_{Di}, u_w, u_o, ρ_o, and u_i are the reference density of the air, a roughness coefficient for the ocean, a roughness coefficient for the ice, the 10-m wind velocity, the first layer ocean velocity, the reference density of the ocean, and the sea ice velocity, respectively. The surface stress (τ_x and τ_y) is computed individually for the u and v components of the velocity . We note that C_{Do} is computed by the model for the wind-ocean stress and set to $C_{Di} = 5 \times 10^{-3}$ for the ice-ocean interaction.

Appendix C: Ekman Depth and Ekman Transport

The Ekman Depth, that is, the depth where the Ekman Transport will be effective, is defined as

$$Ek_d = 0.70 * \left(\frac{1}{f} \sqrt{\frac{\overline{\tau_m}}{\rho}} \right), \tag{C1}$$

where 0.70 is a transfer function given by Large et al. (1994), f is the Coriolis parameter, $\overline{\tau_m}$ is the magnitude of the surface stress (see Appendix D) and $\rho = 1,035$ kg/m^3 is the reference density used in the numerical model for this experiment.

The Ekman Transport is defined as

$$T^x_{Ek} = \frac{1}{\rho f} \tau_y dy, \tag{C2}$$

$$T^y_{Ek} = -\frac{1}{\rho f} \tau_x dx, \tag{C3}$$

where τ_x and τ_y are the surface stresses in the x and y directions, respectively; dy is the grid size in the y direction; and dx is the grid size in the x direction. The superscripts, x and y, denote the direction of the transport and the stress.

Appendix D: Correlation Between the Surface Stress and the Transport

The correlation is computed from the magnitude of the surface stress and the integrated volume (freshwater) transport at each point of the domain. The magnitude of the surface stress is defined as

$$\overline{\tau_m} = \sqrt{\tau_x^2 + \tau_y^2}, \tag{D1}$$

where τ_x and τ_y are the total surface stresses in x and y directions, respectively, as described in Appendix B.

The correlation coefficient is thus computed as

$$r(\tau_m, T) = \frac{1}{N-1}\sum_{N=1}^{N}\left(\frac{\overline{\tau_{mi} - \mu_{\tau m}}}{\sigma_{\tau m}}\right)\left(\frac{\overline{T_i - \mu_T}}{\sigma_T}\right), \quad \text{(D2)}$$

where τ_m is the linearly detrended surface stress magnitude; T the linearly detrendred transport; μ and σ are the mean and standard deviation of τ_m and T, respectively. This is performed at each grid point individually.

Both the magnitude of the surface stress and the integrated transport are detrended to remove all influence of the slow drift that is common in most regional numerical models. The purpose of this study is to analyze how the sea ice dynamics impacts the transport. Consequently, using the magnitude of the stress instead of the individual direction gives a more direct indication by showing if the surface stress increases or decreases the integrated transport through each considered gate.

Acknowledgments
For access to the model output, visit http://knossos.eas.ualberta.ca/anha/. Processing of the CryoSat-2 is funded by the German Ministry of Economics Affairs and Energy (grant: 50EE1008), and data from 2011 to 2017 are obtained from http://www.meereisportal.de (grant: REKLIM-2013-04). The Barrow Strait data from provided by Simon Prinsenberg and the Nares Strait data by Andreas Münchow. This work was funded by NSERC through a Discovery Grant Award (RGPIN 04357), an ENGAGE Grant (EGP 514588-17), as well as the Canadian Arctic Geotraces Program (433848-2012). The experiments have been ran on a Jasper, a Compute Canada computational cluster. We thank the two anonymous reviewers for their input and the discussion that improved the quality of this paper.

References

Amante, C., & Eakins, B. (2009). ETOPO1 1 arc-minute global relief model: Procedures, data sources and analysis (*NOAA Technical Memorandum NESDIS NGDC-24*). Boulder, Colorado: National Geophysical Data Center. https://doi.org/10.7289/V5C8276M

Bailey, W. B. (1957). Oceanographic features of the Canadian Archipelago. *Journal of the Fisheries Research Board of Canada*, *14*(5), 731–769. https://doi.org/10.1139/f57-030

Bamber, J., van den Broeke, M., Ettema, J., Lenaerts, J., & Rignot, E. (2012). Recent large increases in freshwater fluxes from Greenland into the North Atlantic. *Geophysical Research Letters*, *39*, L19501. https://doi.org/10.1029/2012GL052552

Blanke, B., & Delecluse, P. (1993). Variability of the Tropical Atlantic Ocean simulated by a general circulation model with two different mixed-layer physics. *Journal of Physical Oceanography*, *23*(7), 1363–1388. https://doi.org/10.1175/1520-0485(1993)023<1363:VOTTAO>2.0.CO;2

Castro de la Guardia, L., Hu, X., & Myers, P. G. (2015). Potential positive feedback between greenland ice sheet melt and Baffin Bay heat content on the west Greenland shelf. *Geophysical Research Letters*, *42*, 4922–4930. https://doi.org/10.1002/2015GL064626

Collin, A. E. (1962). *The waters of the Canadian Arctic Archipelago*. Nova Scotia: Bedford Institute of Oceanography.

Comiso, J. C. (2000, updated 2015). *Bootstrap sea ice concentration from Nimbus-7 SMMR and DMSP SSM/I, version 2 [2002–2016]*. Boulder, CO: NASA DAAC at National Snow and Ice Data Centre.

Comiso, J. C. (2012). Large decadal decline of the Arctic multiyear ice cover. *Journal of Climate*, *25*(4), 1176–1193. https://doi.org/10.1175/jcli-d-11-00113.1

Comiso, J. C., Meier, W. N., & Gersten, R. (2017). Variability and trends in the Arctic sea ice cover: Results from different techniques. *Journal of Geophysical Research: Oceans*, *122*, 6883–6900. https://doi.org/10.1002/2017JC012768

Cuny, J., Rhines, P. B., & Kwok, R. (2005). Davis Strait volume, freshwater and heat fluxes. *Deep Sea Research Part I: Oceanographic Research Papers*, *52*(3), 519–542. https://doi.org/10.1016/j.dsr.2004.10.006

Curry, B., Lee, C. M., & Petrie, B. (2011). Volume, freshwater, and heat fluxes through Davis Strait, 2004–05*. *Journal of Physical Oceanography*, *41*(3), 429–436. https://doi.org/10.1175/2010jpo4536.1

Curry, B., Lee, C. M., Petrie, B., Moritz, R. E., & Kwok, R. (2014). Multiyear volume, liquid freshwater, and sea ice transports through Davis Strait, 2004–10*. *Journal of Physical Oceanography*, *44*(4), 1244–1266. https://doi.org/10.1175/jpo-d-13-0177.1

Dai, A., Qian, T., Trenberth, K. E., & Milliman, J. D. (2009). Changes in continental freshwater discharge from 1948 to 2004. *Journal of Climate*, *22*(10), 2773–2792. https://doi.org/10.1175/2008jcli2592.1

Fissel, D. B. (1988). Non-tidal flows in the Northwest Passage. *Canadian Technical Report of Hydrography and Ocean Sciences, 98* (143 pp.). Sidney, B.C., Canada: Institute of Ocean Science.

Galley, R. J., Else, B. G. T., Howell, S. E. L., Lukovich, J. V., & Barber, D. G. (2012). Landfast Sea Ice Conditions in the Canadian Arctic: 1983–2009. *Arctic*, *65*(2), 133–144. https://doi.org/10.14430/arctic4195

Grivault, N., Hu, X., & Myers, P. G. (2017). Evolution of Baffin Bay water masses and transports in a numerical sensitivity experiment under enhanced Greenland melt. *Atmosphere-Ocean*, *55*(3), 169–194. https://doi.org/10.1080/07055900.2017.1333950

Haas, C., & Howell, S. E. L. (2015). Ice thickness in the Northwest Passage. *Geophysical Research Letters*, *42*, 7673–7680. https://doi.org/10.1002/2015GL065704

Hannah, C. G., Dupont, F., & Dunphy, M. (2009). Polynyas and Tidal Currents in the Canadian Arctic Archipelago. ARCTIC, [S.l.], v. 62, n. 1, p. 83–95, sep. 2009. https://doi.org/10.14430/arctic115

Houssais, M.-N., & Herbaut, C. (2011). Atmospheric forcing on the Canadian Arctic Archipelago freshwater outflow and implications for the Labrador Sea variability. *Journal of Geophysical Research*, *116*, C00D02. https://doi.org/10.1029/2010JC006323

Howell, S. E. L., Duguay, C. R., & Markus, T. (2009). Sea ice conditions and melt season duration variability within the Canadian Arctic Archipelago: 1979–2008. *Geophysical Research Letters*, *36*, L10502. https://doi.org/10.1029/2009GL037681

Howell, S. E. L., Laliberté, F., Kwok, R., Derksen, C., & King, J. (2016). Landfast ice thickness in the Canadian Arctic Archipelago from observations and models. *The Cryosphere*, *10*(4), 1463–1475. https://doi.org/10.5194/tc-10-1463-2016

Howell, S. E. L., Wohlleben, T., Dabboor, M., Derksen, C., Komarov, A., & Pizzolato, L. (2013). Recent changes in the exchange of sea ice between the Arctic Ocean and the Canadian Arctic Archipelago. *Journal of Geophysical Research: Oceans*, *118*, 3595–3607. https://doi.org/10.1002/jgrc.20265

Hu, X., & Myers, P. G. (2014). Changes to the Canadian Arctic Archipelago sea ice and freshwater fluxes in the twenty-first century under the Intergovernmental Panel on Climate Change A1B climate scenario. *Atmosphere-Ocean*, *52*(4), 331–350. https://doi.org/10.1080/07055900.2014.942592

Hu, X., Sun, J., Chan, T. O., & Myers, P. G. (2018). Thermodynamic and dynamic ice thickness contributions in the Canadian Arctic Archipelago in NEMO-LIM2 numerical simulations. *The Cryosphere*, *12*(4), 1233–1247. https://doi.org/10.5194/tc-12-1233-2018

Hughes, K. G., Klymak, J. M., Hu, X., & Myers, P. G. (2017). Water mass modification and mixing rates in a 1/12° simulation of the Canadian Arctic Archipelago. *Journal of Geophysical Research: Oceans*, *122*, 803–820. https://doi.org/10.1002/2016JC012235

Hunke, E. C. (2001). Viscous–plastic sea ice dynamics with the EVP model: Linearization issues. *Journal of Computational Physics*, *170*(1), 18–38. https://doi.org/10.1006/jcph.2001.6710

Jahn, A., Tremblay, B., Mysak, L. A., & Newton, R. (2009). Effect of the large-scale atmospheric circulation on the variability of the Arctic Ocean freshwater export. *Climate Dynamics*, *34*(2-3), 201–222. https://doi.org/10.1007/s00382-009-0558-z

Kiilerich, A. B. (1939). *The Godthaab Expedition, 1928: A theoretical treatment of the hydrographical observation material*. CA Reitzel Forlag: Kobenhavn.

Kliem, N., & Greenberg, D. A. (2003). Diagnostic simulations of the summer circulation in the Canadian Arctic Archipelago. *Atmosphere-Ocean*, *41*(4), 273–289. https://doi.org/10.3137/ao.410402

Kwok, R., & Rothrock, D. A. (2009). Decline in Arctic sea ice thickness from submarine and ICESat records: 1958–2008. *Geophysical Research Letters*, *36*, L15501. https://doi.org/10.1029/2009GL039035

Large, W. G., McWilliams, J. C., & Doney, S. C. (1994). Oceanic vertical mixing: A review and a model with a nonlocal boundary layer parameterization. *Reviews of Geophysics*, *32*(4), 363–403. https://doi.org/10.1029/94RG01872

Lemieux, J.-F., Dupont, F., Blain, P., Roy, F., Smith, G. C., & Flato, G. M. (2016). Improving the simulation of landfast ice by combining tensile strength and a parameterization for grounded ridges. *Journal of Geophysical Research: Oceans*, *121*, 7354–7368. https://doi.org/10.1002/2016JC012006

Lindsay, R., & Schweiger, A. J. (2013, updated 2017). *Unified sea ice thickness climate data record, 1947 Onward, version 1. [ICESat1-G and CryoSat-AWI]*. Boulder, Colorado USA: NSIDC: National Snow and Ice Data Center. https://doi.org/10.7265/N5D50JXV

Lu, Y., Higginson, S., Nudds, S., Prinsenberg, S., & Garric, G. (2014). Model simulated volume fluxes through the Canadian Arctic Archipelago and Davis Strait: Linking monthly variations to forcing in different seasons. *Journal of Geophysical Research: Oceans*, *119*, 1927–1942. https://doi.org/10.1002/2013JC009408

Madec, G. (2008). Nemo ocean engine. *Note du Pole de modelisation*, *27*, 1288–1619.

Madec, G., Delécluse, P., Imbard, M., & Lévy, C. (1998). OPA 8.1 Ocean General Circulation Model—reference manual. Notes du pôle de modélisation, laboratoire d'océanographie dynamique et de climatologie, Institut Pierre Simon Laplace des sciences de l'environnement global. 11.

Manucharyan, G. E., & Spall, M. A. (2016). Wind-driven freshwater buildup and release in the Beaufort Gyre constrained by mesoscale eddies. *Geophysical Research Letters*, *43*, 273–282. https://doi.org/10.1002/2015GL065957

Manucharyan, G. E., Spall, M. A., & Thompson, A. F. (2016). A theory of the wind-driven Beaufort Gyre variability. *Journal of Physical Oceanography*, *46*(11), 3263–3278. https://doi.org/10.1175/jpo-d-16-0091.1

Masina, S., Storto, A., Ferry, N., Valdivieso, M., Haines, K., Balmaseda, M., et al. (2015). An ensemble of eddy-permitting global ocean reanalyses from the MyOcean project. *Climate Dynamics*, *49*, 813–841. https://doi.org/10.1007/s00382

McGeehan, T., & Maslowski, W. (2012). Evaluation and control mechanisms of volume and freshwater export through the Canadian Arctic Archipelago in a high-resolution pan-Arctic ice-ocean model. *Journal of Geophysical Research*, *117*, C00D14. https://doi.org/10.1029/2011JC007261

Melling, H. (2002). Sea ice of the northern Canadian Arctic Archipelago. *Journal of Geophysical Research*, *107*(C11), 3181. https://doi.org/10.1029/2001JC001102

Melling, H., Agnew, T. A., Falkner, K. K., Greenberg, D. A., Lee, C. M., Münchow, A., et al. (2008). *Fresh-water fluxes via Pacific and Arctic outflows across the Canadian Polar Shelf*. Netherlands: Springer. pp. 193–247.

Münchow, A. (2016). Volume and freshwater flux observations from Nares Strait to the west of Greenland at daily time scales from 2003 to 2009. *Journal of Physical Oceanography*, *46*(1), 141–157. https://doi.org/10.1175/JPO-D-15-0093.1

Münchow, A., & Melling, H. (2008). Ocean current observations from Nares Strait to the west of Greenland: Interannual to tidal variability and forcing. *Journal of Marine Research*, *66*(6), 801–833.

Palfrey, K., & Day, G. (1968). Oceanography of Baffin Bay and Nares Strait in the summer of 1966. *USCG Oceanographie Rep*, *16*, 1–74.

Parkinson, C. L., & Cavalieri, D. J. (2008). Arctic sea ice variability and trends, 1979–2006. *Journal of Geophysical Research*, *113*, C07003. https://doi.org/10.1029/2007JC004558

Parkinson, C. L., & Comiso, J. C. (2013). On the 2012 record low Arctic sea ice cover: Combined impact of preconditioning and an August storm. *Geophysical Research Letters*, *40*, 1356–1361. https://doi.org/10.1002/grl.50349

Peterson, I., Hamilton, J., Prinsenberg, S., & Pettipas, R. (2012). Wind-forcing of volume transport through Lancaster Sound. *Journal of Geophysical Research*, *117*, C11018. https://doi.org/10.1029/2012JC008140

Prinsenberg, S., & Bennett, E. (1987). Mixing and transports in Barrow Strait, the central part of the Northwest passage. *Continental Shelf Research*, *7*(8), 913–935. https://doi.org/10.1016/0278-4343(87)90006-9

Prinsenberg, S., Hamilton, J., Peterson, I., & Pettipas, R. (2009). Observing and interpreting the seasonal variability of the oceanographic fluxes passing through Lancaster Sound of the Canadian Arctic Archipelago, *Influence of Climate Change on the Changing Arctic and Sub-Arctic Conditions* (pp. 125–143). Netherlands: Springer.

Ryan, P. A., & Münchow, A. (2017). Sea ice draft observations in Nares Strait from 2003 to 2012. *Journal of Geophysical Research: Oceans*, *122*, 3057–3080. https://doi.org/10.1002/2016JC011966

Shroyer, E. L., Samelson, R. M., Padman, L., & Münchow, A. (2015). Modeled ocean circulation in Nares Strait and its dependence on landfast-ice cover. *Journal of Geophysical Research: Oceans*, *120*, 7934–7959. https://doi.org/10.1002/2015JC011091

Smith, G. C., Roy, F., Mann, P., Dupont, F., Brasnett, B., Lemieux, J.-F., et al. (2014). A new atmospheric dataset for forcing ice-ocean models: Evaluation of reforecasts using the Canadian global deterministic prediction system. *Quarterly Journal of the Royal Meteorological Society*, *140*(680), 881–894. https://doi.org/10.1002/qj.2194

Sou, T., & Flato, G. (2009). Sea ice in the Canadian Arctic Archipelago: Modeling the past (1950–2004) and the future (2041–60). *Journal of Climate*, *22*(8), 2181–2198. https://doi.org/10.1175/2008JCLI2335.1

Spence, C., & Burke, A. (2008). Estimates of Canadian Arctic Archipelago runoff from observed hydrometric data. *Journal of Hydrology*, *362*(3-4), 247–259. https://doi.org/10.1016/j.jhydrol.2008.08.019

Stroeve, J., Holland, M. M., Meier, W., Scambos, T., & Serreze, M. (2007). Arctic sea ice decline: Faster than forecast. *Geophysical Research Letters*, *34*, L09501. https://doi.org/10.1029/2007GL029703

Tang, C. C., Ross, C. K., Yao, T., Petrie, B., DeTracey, B. M., & Dunlap, E. (2004). The circulation, water masses and sea-ice of Baffin Bay. *Progress in Oceanography*, *63*(4), 183–228. https://doi.org/10.1016/j.pocean.2004.09.005

Vancoppenolle, M., Fichefet, T., Goosse, H., Bouillon, S., Madec, G., & Maqueda, M. A. M. (2009). Simulating the mass balance and salinity of Arctic and Antarctic sea ice. 1. Model description and validation. *Ocean Modelling*, *27*(1–2), 33–53. https://doi.org/10.1016/j.ocemod.2008.10.005

Wang, Z., Hamilton, J., & Su, J. (2017). Variations in freshwater pathways from the Arctic Ocean into the North Atlantic Ocean. *Progress in Oceanography*, *155*, 54–73. https://doi.org/10.1016/j.pocean.2017.05.012

Wang, Q., Myers, P. G., Hu, X., & Bush, A. B. (2012). Flow constraints on pathways through the Canadian Arctic Archipelago. *Atmosphere-Ocean*, *50*(3), 373–385. https://doi.org/10.1080/07055900.2012.704348

Wekerle, C., Wang, Q., Danilov, S., Jung, T., & Schröter, J. (2013). The Canadian Arctic Archipelago throughflow in a multiresolution global model: Model assessment and the driving mechanism of interannual variability. *Journal of Geophysical Research: Oceans*, *118*, 4525–4541. https://doi.org/10.1002/jgrc.20330

Yang, Q., Dixon, T. H., Myers, P. G., Bonin, J., Chambers, D., van den Broeke, M. R., et al. (2016). Corrigendum: Recent increases in Arctic freshwater flux affects Labrador Sea convection and Atlantic overturning circulation. *Nature Communications*, *7*, 13545. https://doi.org/10.1038/ncomms13545

Zhang, Y., Chen, C., Beardsley, R. C., Gao, G., Lai, Z., Curry, B., et al. (2016). Studies of the Canadian Arctic Archipelago water transport and its relationship to basin-local forcings: Results from AO-FVCOM. *Journal of Geophysical Research: Oceans*, *121*, 4392–4415. https://doi.org/10.1002/2016JC011634